Femtosecond X-Ray Scattering Study of Ultrafast Photoinduced Structural Dynamics in Solvated $[Co(terpy)_2]^{2+}$

Elisa Biasin,[1] Tim Brandt van Driel,[1] Kasper S. Kjær,[1,2,3] Asmus O. Dohn,[4] Morten Christensen,[1] Tobias Harlang,[2] Pavel Chabera,[2] Yizhu Liu,[2,5] Jens Uhlig,[2] Mátyás Pápai,[4,6] Zoltán Németh,[6] Robert Hartsock,[3] Winnie Liang,[3] Jianxin Zhang,[7] Roberto Alonso-Mori,[8] Matthieu Chollet,[8] James M. Glownia,[8] Silke Nelson,[8] Dimosthenis Sokaras,[8] Tadesse A. Assefa,[9] Alexander Britz,[9] Andreas Galler,[9] Wojciech Gawelda,[9,10] Christian Bressler,[9] Kelly J. Gaffney,[3] Henrik T. Lemke,[8,11] Klaus B. Møller,[4] Martin M. Nielsen,[1] Villy Sundström,[2] György Vankó,[6] Kenneth Wärnmark,[5] Sophie E. Canton,[12,13] and Kristoffer Haldrup[1,*]

[1]*Department of Physics, Technical University of Denmark, Fysikvej 307, DK-2800 Kongens Lyngby, Denmark*
[2]*Department of Chemical Physics, Lund University, Box 118, S-22100 Lund, Sweden*
[3]*PULSE Institute, SLAC National Accelerator Laboratory, Menlo Park, California 94025, USA*
[4]*Department of Chemistry, Technical University of Denmark, Kemitorvet 207, DK-2800 Kongens Lyngby, Denmark*
[5]*Centre for Analysis and Synthesis, Department of Chemistry, Lund University, Box 124, Lund SE-22100, Sweden*
[6]*Wigner Research Centre for Physics, Hungarian Academy Sciences, H-1525 Budapest, Hungary*
[7]*School of Environmental and Chemical Engineering, Tianjin Polytechnic University, Tianjin 300387, China*
[8]*LCLS, SLAC National Accelerator Laboratory, Menlo Park, California 94025, USA*
[9]*European XFEL GmbH, Albert-Einstein-Ring 19, D-22761 Hamburg, Germany*
[10]*Institute of Physics, Jan Kochanowski University, 25-406 Kielce, Poland*
[11]*SwissFEL, Paul Scherrer Institut, 5232 Villigen PSI, Switzerland*
[12]*IFG Structural Dynamics of (Bio)chemical Systems, Max Planck Institute for Biophysical Chemistry, Am Fassberg 11, D-37077 Goettingen, Germany*
[13]*FS-SCS, Structural Dynamics with Ultra-short Pulsed X-rays, Deutsches Elektronen-Synchrotron (DESY), Notkestrasse 85, D-22607 Hamburg, Germany*

(Received 5 February 2016; published 30 June 2016)

We study the structural dynamics of photoexcited $[Co(terpy)_2]^{2+}$ in an aqueous solution with ultrafast x-ray diffuse scattering experiments conducted at the Linac Coherent Light Source. Through direct comparisons with density functional theory calculations, our analysis shows that the photoexcitation event leads to elongation of the Co-N bonds, followed by coherent Co-N bond length oscillations arising from the impulsive excitation of a vibrational mode dominated by the symmetrical stretch of all six Co-N bonds. This mode has a period of 0.33 ps and decays on a subpicosecond time scale. We find that the equilibrium bond-elongated structure of the high spin state is established on a single-picosecond time scale and that this state has a lifetime of ~7 ps.

DOI: 10.1103/PhysRevLett.117.013002

Several Co(II) compounds are known to transition between their low spin (LS) and high spin (HS) electronic states [1–3]. Such transitions can be induced by temperature increase, excitation by light, or high magnetic fields [4], and they are accompanied by distinct changes in magnetic and structural properties that may be exploited in the design of display and memory devices [5,6] and in single-molecule spintronic applications [7]. The realization of exploitable spin-state transitions (SSTs) in Co(II) compounds is more challenging than in the corresponding Fe(II) complexes, which have been investigated in great detail during the last decades [8–15]. These challenges stem from the partial occupation of the antibonding e_g^* orbitals in the ground state, which leads to smaller structural changes arising from the SST phenomenon; the corresponding smaller energy barriers between the potential surfaces of the HS and LS Co(II) states result in faster dynamics [1], as well as a high sensitivity to the crystalline environment or to the solvent properties [2]. The key structural parameters for the SSTs are the Co-N bond lengths [8], but the time scales and the dynamics of the LS-HS transitions have remained unclear for Co compounds. Time-resolved x-ray scattering can be used to monitor such structural changes and dynamics if the time resolution of the experiment is sufficiently high. X-ray free electron lasers (XFELs) provide ultrashort (~30 fs) x-ray pulses and high flux allowing the nuclear dynamics following photoexcitation to be recorded at the required femtosecond time scales [16,17]. Here, we report, for the first time, direct measurements of the excited-state structure and the ultrafast structural dynamics of a solvated Co(II) complex upon a photoinduced SST.

Figure 1 shows the molecular structure of $[Co(terpy)_2]^{2+}$ (terpy $= 2,2':6',2''-$ terpyridine). In this six-coordinated complex, the d^7 Co center can be either a LS doublet state or a HS quartet state [2,18]. In solid-state samples, the relative populations of both spin states depend strongly on the

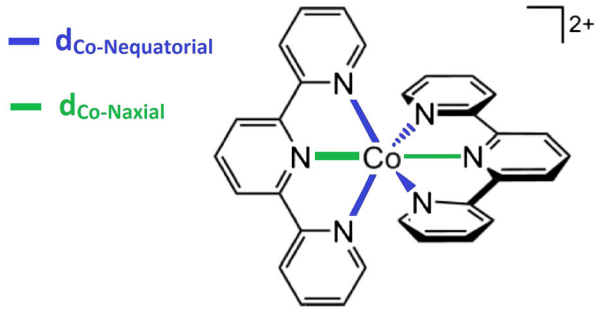

FIG. 1. Schematic representation of the structure of $[Co(terpy)_2]^{2+}$. The LS → HS transition can be induced by photoexcitation with a 530 nm laser pulse and is characterized by an anisotropic expansion of the metal-ligand bonds. Axial and equatorial Co-N bonds are highlighted in different colors.

temperature and on the crystalline environment [19–21]. In crystallographic studies the compound was observed to be compressed in the LS state (short axial and long equatorial Co-N bonds), due mostly to the geometrical constraints of the coordinating tridentate ligands, and may also exhibit asymmetry, with one ligand being closer to the Co center than the other due to a pseudo–Jahn-Teller effect [20,22]. Upon LS → HS transition in solid-state samples, the axial bond length has been observed to increase by up to 0.21 Å and the equatorial by 0.07 Å, depending on the anion and the degree of hybridization [23]. As reported by Vargas *et al.* [22], density functional theory (DFT) calculations in the gas phase also predict an anisotropic increase of the Co-N bonds upon the LS → HS spin change (an increase of 0.16 and 0.05 Å for the axial and equatorial bonds, respectively). A few studies on the properties of $[Co(terpy)_2]^{2+}$ in solution also exist [2,3,18,24]. Kremer *et al.* [18] report that solvated $[Co(terpy)_2]^{2+}$ is predominantly LS at room temperature, and Enachescu *et al.* demonstrated that photoexcitation in the visible range populates the metal to ligand charge transfer (MLCT) state from which the HS state is populated [3]. Very little information is available regarding the excited-state decay pathways and the HS → LS relaxation time is currently only known to be less than 2 ns [24].

In this work, we utilized x-ray diffuse scattering (XDS) laser pump–x-ray probe experiments to study the formation, structure, and decay of the HS state of aqueous $[Co(terpy)_2]^{2+}$. The measurements were conducted at the x-ray pump-probe (XPP) instrument at the Linac Coherent Light Source (LCLS) XFEL facility [17]. A 20 mM aqueous solution of $[Co(terpy)_2]^{2+}$ was pumped trough a nozzle producing a 100 μm liquid sheet flowing in the vertical direction at a flow rate sufficient to fully replace the sample between successive pump-probe events. The photocycle was initiated by 70 μJ laser pulses at 530 nm and with a 70 fs pulse width (FWHM) focused onto a spot of 150 μm (FWHM). The 8.3 keV x-ray probe pulses overlapped with the pump laser at the sample position. The time delay t between the laser and the x-ray pulses was determined for every pump-probe event with ∼10 fs (FWHM) resolution using the XPP timing tool [25]. The scattered x-rays were detected by a Cornell-SLAC pixel array detector [26] 70 mm after the sample, covering scattering vectors Q up to 3.5 $Å^{-1}$.

Following detector corrections [27], the scattering signal was scaled to the liquid unit cell reflecting the stoichiometry of the sample [28], yielding the acquired signal in electron units per solute molecule (e.u./molec). Individual 2D difference scattering patterns were obtained by subtracting images where the pump laser was dropped before the sample from those where the pump laser had interacted

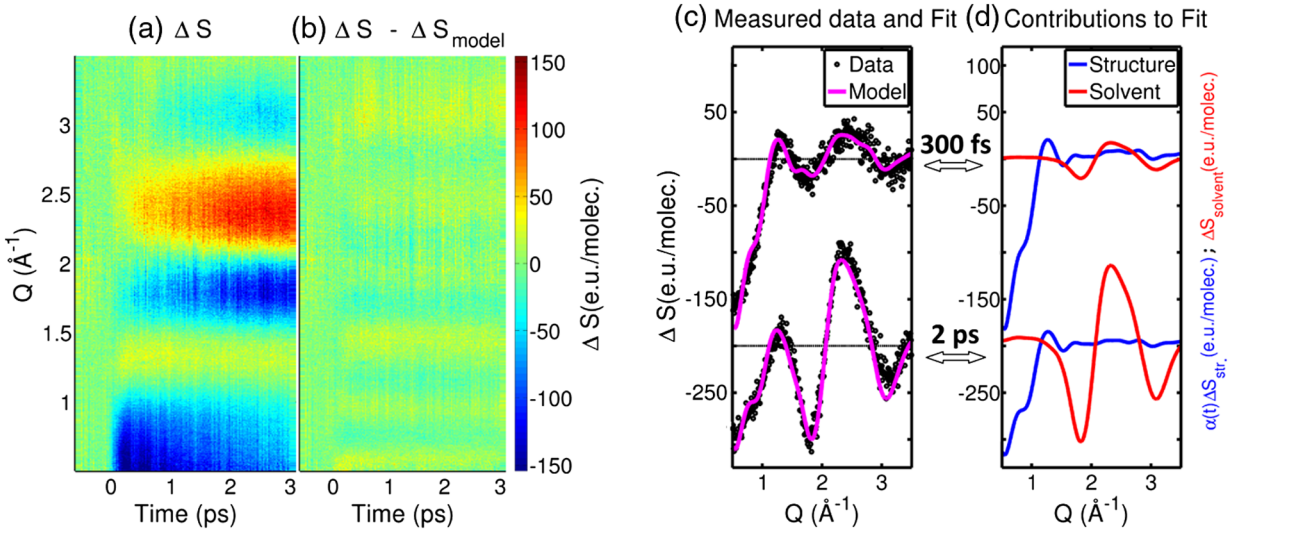

FIG. 2. (a) Measured difference scattering signal (ΔS) of photoexcited $[Co(terpy)_2]^{2+}$ in water. (b) Residuals obtained by subtracting the model (ΔS_{model}) from the experimental data. (c),(d) Fit of the 1D difference scattering curves at 300 fs and 2 ps. (c) The modeled difference signal (the magenta line) overlaid over the experimental data (the black points). (d) The contributions to the model from the structural changes (solute and cage, the blue line) and from the bulk solvent (the red line).

with the sample. The patterns were then time sorted and averaged in ~23 fs wide bins. Finally, 1D isotropic and anisotropic difference scattering signals were extracted [29]. Figure 2(a) shows the measured isotropic difference signals $\Delta S(Q,t)$ in a 2D representation.

$\Delta S(Q,t)$ can be considered as arising from three contributions [30]: the structural changes in the solute molecules (ΔS_{solute}), the local changes in geometry and rearrangements of the solvent molecules in close proximity to the solute (ΔS_{cage}), and the temperature and density changes in the bulk solvent following energy deposition ($\Delta S_{\text{solvent}}$).

$\Delta S_{\text{solute}}(Q)$ can be directly calculated from putative structural models of the molecule through the Debye equation [Eq. (S2) in the Supplemental Material (SM) [31]]. As a starting point for the present analysis, the difference scattering signal expected upon the photoexcitation was calculated from the LS and HS DFT-optimized geometries of $[\text{Co(terpy)}_2]^{2+}$:

$$\Delta S_{\text{solute}}(Q) = S_{\text{HS}}(Q) - S_{\text{LS}}(Q). \quad (1)$$

The DFT calculations were carried out as detailed in the SM [31], and Table I reports the key DFT-calculated structural parameters. Upon the LS → HS transition, the Co-N bonds expand ~0.16 and ~0.08 Å along the axial and the equatorial directions, respectively, in good agreement with the earlier study by Vargas *et al.* [22]. The ratio between the axial and the equatorial Co-N disatnce is defined as η. In the LS state the average η is 0.91 (0.88 and 0.92 for the two ligands, with the difference due to the Jahn-Teller effect), while in the HS state η increases to 0.95 (for both ligands).

The cage contribution $\Delta S_{\text{cage}}(Q)$ to the simulated signal was calculated from the radial distribution functions of the solute-solvent atom pairs [43] determined through classical molecular dynamics (MD) simulations [31]. The contribution from changes in the solute structure and the solvation cage are related 1:1 and can therefore be combined under the term "structure", $\Delta S_{\text{str.}}(Q)$, such that

$$\Delta S_{\text{str.}}(Q) = \Delta S_{\text{solute}}(Q) + \Delta S_{\text{cage}}(Q). \quad (2)$$

Finally, the bulk-solvent term $\Delta S_{\text{solvent}}(Q)$ has been shown to be very well described by a linear combination of solvent difference signals, $(\partial S(Q)/\partial T)|_\rho$ and $(\partial S(Q)/\partial \rho)|_T$, which can be measured in separate experiments [44,45]:

$$\Delta S(Q,t)_{\text{solvent}} = \Delta T(t)\left.\frac{\partial S(Q)}{\partial T}\right|_\rho + \Delta\rho(t)\left.\frac{\partial S(Q)}{\partial \rho}\right|_T, \quad (3)$$

where ΔT and $\Delta\rho$ are the changes in temperature and density, respectively. Such solvent differentials for XDS experiments are archived for a range of solvents [45,46] and are used in the present work. In contrast to earlier experiments on Fe SST compounds [30], we observe no density change above our detection limit of 0.05 kg/m^3 [Fig. S1(b) of the SM [31]], and this term was thus excluded from the analysis.

From visual inspection of the measured difference signal in Fig. 2(a), we qualitatively observe a very fast rise of a negative feature at low Q ($Q < 1$ Å^{-1}) which gradually decays over the course of several picoseconds. Such a low-Q feature is characteristic of an increase in the solute size. On the few picosecond time scale, a distinct signal around $Q = 2$ Å^{-1} grows in. This feature is identified as the characteristic difference signal arising from a temperature increase of the aqueous solvent. In the low-Q region, oscillatory features as a function of time can be observed and indicate structural dynamics along the main coordinate of the structural changes; in the present case, the Co-N bond lengths ($d_{\text{Co-N}}$). The latter is therefore introduced as a time-dependent parameter in Eq. (1):

$$S_{\text{HS}}(Q,t) = S_{\text{HS}}(Q, d_{\text{Co-N}}(t)). \quad (4)$$

Specifically, $d_{\text{Co-Naxial}}$ of the HS structure was allowed to vary ±0.1 Å from the value reported in Table I, while the ratio η, through which $d_{\text{Co-Nequatorial}}$ can be calculated and included in the structural modeling, was kept fixed to 0.95 in the analysis. Thus, all six Co-N bond length changes are parametrized through the single structural parameter $d_{\text{Co-Naxial}}$.

Based on the considerations outlined above, the full model applied to fit and interpret the measured difference signal is thus:

$$\Delta S_{\text{model}}(Q,t) = \alpha(t)\Delta S_{\text{str.}}(Q,t) + \Delta T(t)\left.\frac{\partial S(Q)}{\partial T}\right|_\rho, \quad (5)$$

where $\alpha(t)$ describes the time-dependent excitation fraction of the solute, which, in the context of the present analysis, is assumed to be described by an exponential decay starting at t_0, i.e., the arrival time of the laser pump. The time resolution of the experiment is included by convolution with the (Gaussian) instrument response function (IRF) to yield the following expression for $\alpha(t)$:

$$\alpha(t) = \text{IRF}(\sigma_{\text{IRF}}, t) \otimes H(t - t_0)Ae^{-(t-t_0/\tau)}, \quad (6)$$

TABLE I. Structural parameters of the DFT-calculated LS and HS structures of $[\text{Co(terpy)}_2]^{2+}$ obtained in the present study. $d_{\text{Co-Naxial}}$ and $d_{\text{Co-Nequatorial}}$ are averages over the two axial and the four equatorial metal-ligand bond distances, respectively, and $\eta = (d_{\text{Co-Naxial}}/d_{\text{Co-Nequatorial}})$. The change of each parameter upon the LS → HS spin transition is also reported and compared with the values obtained from the measured data.

	LS	HS		DFT	Measured
$d_{\text{Co-Naxial}}$ (Å)	1.902	2.058	$\Delta d_{\text{Co-Naxial}}$ (Å)	0.16	0.13
$d_{\text{Co-Nequatorial}}$ (Å)	2.08	2.16	$\Delta d_{\text{Co-Nequatorial}}$ (Å)	0.08	0.06
η	0.91	0.95			

where σ_{IRF} is the width of the IRF; A and τ are the amplitude and the lifetime of the exponential function representing, respectively, the initial excitation fraction and the lifetime of the bond-elongated excited state; and H is the Heaviside step function centered at t_0 [as detailed in Eq. (S3) of the SM [31]]. We note that assuming the excited-state population to be given by the integral of a Gaussian envelope of the excitation pulse is an approximation—especially given the high intensity of the optical excitation, as discussed in further detail below. σ_{IRF} and t_0 were determined from the transient solvent contribution to the anisotropic part of the difference scattering signal (Fig. S4 of the SM [31]), from which we find $\sigma_{\mathrm{IRF}} = 0.05$ ps $\pm$ 0.03 ps. Furthermore, we estimated the lifetime of the HS state from a single set of measurements out to 20 ps. The analysis of this data set is presented in the SM and yields $\tau = 6.8$ ps $\pm$ 0.8 ps [Fig. S8(a) of the SM [31]], allowing us to constrain this parameter in Eq. (6).

From these considerations, the number of free parameters in the model described by Eq. (5) is reduced to three: A, $d_{\mathrm{Co\text{-}Naxial}}$, and ΔT. The model was fitted to the acquired difference signal $\Delta S(Q)$ for all time delays simultaneously within a standard χ^2 [Eq. (S6) of the SM [31]] minimization framework [47]. Good fits were observed for all time delays, and Fig. 2(b) shows the residuals after subtracting the model from the measured data. Figures 2(c) and 2(d) show examples of the fitting results at two time delays, 300 fs and 2 ps.

From the kinetics part of the fit of our model to the acquired data, the initial excitation fraction A was found to be 34% $\pm$ 2%. Regarding the difference signal arising from solvent heating: the analysis of $\Delta T(t)$ is discussed in detail in the SM [Figs. S3 and S8(b) [31]], but, stated briefly, it is found to be well described by a broadened double exponential dominated (> 90%) by a response with a grow-in time constant of 4.0 ps $\pm$ 0.6 ps. A total solvent temperature increase of $\Delta T = 0.8$ K is found, which is 0.4 K more than the amount of energy expected to be released through nonradiative decay processes after single-photon excitation of the solute. As detailed in the SM [31], this extra heat can be ascribed to multiphoton absorption due to the relatively high excitation laser intensity and short pulse length. A direct comparison with data taken at 3 times lower laser power (Fig. S10 of the SM [31]) shows that the multiphoton absorption has no discernible impact on the structural response of the solute molecules.

Turning to the key results of this Letter, Fig. 3 shows the best-fit result for the changes in $d_{\mathrm{Co\text{-}Naxial}}$ from the ground to the excited state as a function of time (the black data points). Following excitation, the axial Co-N bond increases by $\Delta d_{\mathrm{Co\text{-}Naxial}} = 0.14$ Å and exhibits oscillations. On the 1 ps time scale, the axial Co-N bond length of the excited-state ensemble decreases by ~0.01 Å and then remains constant over the ~7 ps lifetime of the HS state. Thus, $d_{\mathrm{Co\text{-}Naxial}}$ and $d_{\mathrm{Co\text{-}Nequatorial}}$ are found to be, respectively, 0.13 and 0.06 Å longer in the HS state than in the

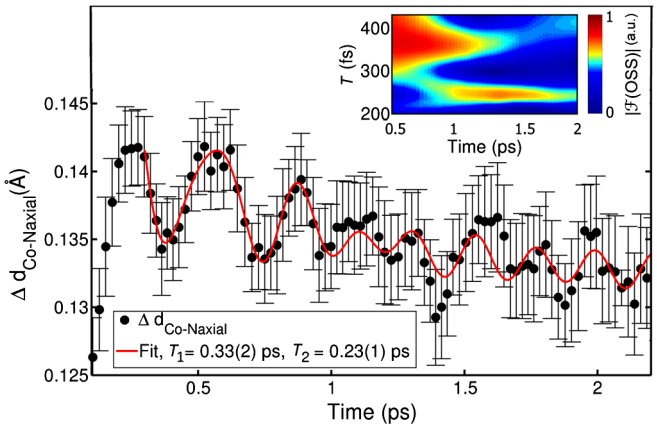

FIG. 3. Time evolution of the Co-N bond lengths (black dots) upon photoexcitation, smoothed with 4-point (~100 fs) moving average filter. The insert shows a time-resolved Fourier transform of the oscillatory part of the difference scattering signal (Fig. 2(a) and Fig. S6 [31]), indicating sequential activation of two vibrational modes. The red line shows a heuristic fit, incorporating sequential activation of first a $T_1 \sim 0.33$ ps mode and then a $T_2 \sim 0.23$ ps mode identified as, respectively, breathing- and pincerlike by direct comparison with our DFT calculations.

LS state, distance changes which are slightly smaller than the DFT predictions (Table I). The rise time of the solvent heating signal indicates that full thermal equilibration with the surrounding solvent takes place in about 4 ps.

The inset of Fig. 3 shows a time-dependent Fourier transform ($\mathcal{F}$) of the oscillatory structural signal contained in ΔS and calculated as detailed in the SM [31]. From this, we observe two distinct components: one mode which appears within the time resolution of our experiment and decays on a ~1 ps time scale, and one mode which grows in after 1 ps. The red line in Fig. 3 illustrates the fit of a heuristic model to the data after the initial lengthening of the Co-N axial bond. The model is comprised of two sinusoidals [Eq. (S4) of the SM [31]], the first one being damped and driving the second. Both sinusoidals are broadened by the IRF and superimposed on an exponentially decaying background with a time constant of 0.7 ps $\pm$ 0.1 ps. From this fit, we find that the period T_1 of the main oscillation is 0.33 ps $\pm$ 0.03 ps and that the damping time is 0.4 ps $\pm$ 0.1 ps. On the same time scale, we observe the growing of the second oscillation with a period of $T_2 = 0.23$ ps $\pm$ 0.01 ps. In the framework of this analysis and by direct comparison with the DFT-calculated vibrational modes of the HS state, we assign the first component to a breathinglike mode (movie S1 of the SM [31]) with synchronous stretching of all six Co-N bonds, whereas the second, weaker component is assigned to arise from a pincerlike movement of the tridentate ligands (movie S2 of the SM [31]). The assignment of these modes is in good agreement with the recent work on related Fe(II) complexes [10,48,49], where the immediately excited stretching modes were quickly damped as energy

was dissipated into other degrees of freedom. Future experiments utilizing higher x-ray energies to access a larger region of momentum space should facilitate detailed studies of the structural degrees of freedom [as recently demonstrated for $[Fe(terpy)_2]^{2+}$ on synchrotron time scales (100 ps) [12,50,51]] involved in the structural relaxation of the electronically excited state. Such studies may be fruitfully combined with *ab initio* MD [52], thus going beyond the classical-mechanics description of the combined DFT-MD simulations used in the present analysis.

Returning to the solute dynamics, by assuming that the excited-state potential is well approximated by a harmonic potential and if the population of this state is nearly instantaneous, one would expect the ensemble mean of the Co-N bond length to reach its maximum value one half period (~0.17 ps) after excitation. From Fig. 3, we find this point to be reached only after 0.25 ps. By singular value decomposition of the structural contribution to ΔS (Figs. S4 and S5 of the SM [31]), we find this observation of a delayed structural transition to be model independent and further find that the delayed onset is well described by an exponential grow-in ($\tau = 0.06$ ps $\pm$ 0.01 ps) of the signal with a 0.08 ps $\pm$ 0.02 ps phase shift of the oscillations. These observations are consistent with the excited-state structural dynamics taking place on several potential surfaces: photoexcitation produces a MLCT excited state, while bond elongation is believed to occur predominantly in the metal-centered HS excited state. Referring back to the discussion of Eq. (6), we note that this expression is only strictly applicable in a regime of linear response and that, therefore, the ~100 fs delay in bond elongation can be considered only a coarse, structural measure of the time scale involved in the electronic processes of intersystem crossing and internal conversion that eventually leads to formation of the HS state. This delay, while sufficiently fast to launch the observed synchronous Co-N stretch mode, leads to a significant broadening of the HS population in terms of the Co-N bond lengths. This in turn leads to the observed phase shift and the comparatively low amplitude of the observed oscillations.

These results demonstrate how time-resolved x-ray scattering with solution-state samples can be utilized to accurately characterize femtosecond structural dynamics as photoexcited molecules traverse the potential energy landscape of the excited state(s). We believe the results and methodology presented here to be broadly applicable, and we envision that these types of experiments will have a significant impact on our understanding of the fundamental mechanisms at work in SST systems and in both natural and artificial photosensitizers, where the redistribution of energy to different and strongly coupled internal degrees of freedom (both electronic and structural) are of key importance.

The DTU-affiliated authors would like to gratefully acknowledge DANSCATT for funding the beam time efforts. M. M. N., K. B. M., K. H., A. D., E. B., K. S. K., and T. B. V. D. acknowledge support from Det Frie Forskningsråd (DFF), and the Lundbeck Foundation. S. E. C acknowledges funding from SFB 1073. This project was also supported by the European Research Council via Contract No. ERC-StG-259709, the Hungarian Scientific Research Fund (OTKA) under Contract No. K29724 and the Lendület (Momentum) Program of the Hungarian Academy of Sciences (LP2013-59). Z. N. acknowledges support from the Bolyai Fellowship of the Hungarian Academy of Sciences. M. P. acknowledges support from the People Programme (Marie Curie Actions) of the European Union's Seventh Framework Programme (FP7 2007–2013) under REA Grant Agreement No. 609405 (COFUNDPostdocDTU). J. U. gratefully acknowledges the continued funding from the Knut and Alice Wallenberg Foundation. J. Z. greatly acknowledges support from NSFC (21302138) and the Tianjin High School Science and Technology Fund Planning Project (20130504). R. W. H., H. W. L., and K. J. G. acknowledge support from the AMOS program within the Chemical Science, Geosciences and Biosciences Division of the Office of Basic Energy Sciences, Office of Science, U.S. Department of Energy. T. A., A. B., W. G., A. G., and C. B. acknowledge funding from the German Science Foundation (DFG) via SFB925 and from the Centre of Ultrafast Imaging (CUI). Use of the Linac Coherent Light Source (LCLS), SLAC National Accelerator Laboratory, is supported by the U.S. Department of Energy, Office of Science, Office of Basic Energy Sciences under Contract No. DE-AC02-76SF00515.

*Corresponding author.
hald@fysik.dtu.dk

[1] H. A. Goodwin, Top. Curr. Chem. **234**, 23 (2004).
[2] I. Krivokapic, M. Zerara, M. L. Daku, A. Vargas, C. Enachescu, C. Ambrus, P. Tregenna-Piggott, N. Amstutz, E. Krausz, and A. Hauser, Coord. Chem. Rev. **251**, 364 (2007).
[3] C. Enachescu, I. Krivokapic, M. Zerara, J. A. Real, N. Amstutz, and A. Hauser, Inorg. Chim. Acta **360**, 3945 (2007).
[4] A. Bousseksou, K. Boukheddaden, M. Goiran, C. Consejo, M.-L. Boillot, and J.-P. Tuchagues, Phys. Rev. B **65**, 172412 (2002).
[5] O. Kahn and C. J. Martinez, Science **279**, 44 (1998).
[6] G. Molnár, L. Salmon, W. Nicolazzi, F. Terki, and A. Bousseksou, J. Mater. Chem. C **2**, 1360 (2014).
[7] E. Ruiz, Phys. Chem. Chem. Phys. **16**, 14 (2014).
[8] P. Gütlich and H. A. Goodwin, Top. Curr. Chem. **233**, 1 (2004).
[9] M. Chergui, in *Spin-Crossover Materials*, edited by M. A. Halcrow (John Wiley & Sons, New York, 2013), p. 405.
[10] M. Cammarata, R. Bertoni, M. Lorenc, H. Cailleau, S. Di Matteo, C. Mauriac, S. F. Matar, H. Lemke, M. Chollet, S. Ravy *et al.*, Phys. Rev. Lett. **113**, 227402 (2014).
[11] G. Vankó, T. Neisius, G. Molnár, F. Renz, S. Kárpáti, A. Shukla, and F. M. F. de Groot, J. Phys. Chem. B **110**, 11647 (2006).

[12] S. E. Canton, X. Zhang, L. M. Lawson Daku, A. L. Smeigh, J. Zhang, Y. Liu, C.-J. Wallentin, K. Attenkofer, G. Jennings, C. A. Kurtz *et al.*, J. Phys. Chem. C **118**, 4536 (2014).
[13] J. Nance, D. N. Bowman, S. Mukherjee, C. T. Kelley, and E. Jakubikova, Inorg. Chem. **54**, 11259 (2015).
[14] K. Haldrup *et al.*, J. Phys. Chem. B **120**, 1158 (2016).
[15] H. Lemke *et al.*, arXiv:1511.01294.
[16] H. T. Lemke, C. Bressler, L. X. Chen, D. M. Fritz, K. J. Gaffney, A. Galler, W. Gawelda, K. Haldrup, R. W. Hartsock, H. Ihee, J. Kim, K. H. Kim, J. H. Lee, M. M. Nielsen, A. B. Stickrath, W. Zhang, D. Zhu, and M. Cammarata, J. Phys. Chem. A **117**, 735 (2013).
[17] M. Chollet, R. Alonso-Mori, M. Cammarata, D. Damiani, J. Defever, J. T. Delor, Y. Feng, J. M. Glownia, J. B. Langton, S. Nelson, K. Ramsey, A. Robert, M. Sikorski, S. Song, D. Stefanescu, V. Srinivasan, D. Zhu, H. T. Lemke, and D. M. Fritz, J. Synchrotron Radiat. **22**, 503 (2015).
[18] S. Kremer, W. Henke, and D. Reinen, Inorg. Chem. **21**, 3013 (1982).
[19] J. S. Judge and W. Baker, Jr., Inorg. Chim. Acta **1**, 68 (1967).
[20] S. Hayami, Y. Komatsu, T. Shimizu, H. Kamihata, and Y. H. Lee, Coord. Chem. Rev. **255**, 1981 (2011).
[21] H. Oshio, H. Spiering, V. Ksenofontov, F. Renz, and P. Gütlich, Inorg. Chem. **40**, 1143 (2001).
[22] A. Vargas, I. Krivokapic, A. Hauser, and L. M. Lawson Daku, Phys. Chem. Chem. Phys. **15**, 3752 (2013).
[23] B. N. Figgis, E. S. Kucharski, and A. H. White, Australian Journal of Chemistry **36**, 1537 (1983).
[24] J. K. Beattie, R. A. Binstead, M. T. Kelso, P. Del Favero, T. G. Dewey, and D. H. Turner, Inorg. Chim. Acta **235**, 245 (1995).
[25] M. P. Minitti, J. S. Robinson, R. N. Coffee, S. Edstrom, S. Gilevich, J. M. Glownia, E. Granados, P. Hering, M. C. Hoffmann, A. Miahnahri *et al.*, J. Synchrotron Radiat. **22**, 526 (2015).
[26] H. T. Philipp, M. Hromalik, M. Tate, L. Koerner, and S. M. Gruner, Nucl. Instrum. Methods Phys. Res., Sect. A **649**, 67 (2011).
[27] T. B. van Driel, K. S. Kjaer, E. Biasin, K. Haldrup, H. T. Lemke, and M. M. Nielsen, Faraday Discuss. **177**, 443 (2015).
[28] K. Haldrup, M. Christensen, and M. Meedom Nielsen, Acta Crystallogr. Sect. A **66**, 261 (2010).
[29] U. Lorenz, K. B. Møller, and N. E. Henriksen, New J. Phys. **12**, 113022 (2010).
[30] K. Haldrup, G. Vankó, W. Gawelda, A. Galler, G. Doumy, A. M. March, E. P. Kanter, A. Bordage, A. Dohn, T. B. van Driel, K. S. Kjær, H. T. Lemke, S. E. Canton, J. Uhlig, V. Sundström, L. Young, S. H. Southworth, M. M. Nielsen, and C. Bressler, J. Phys. Chem. A **116**, 9878 (2012).
[31] See Supplemental Material at http://link.aps.org/supplemental/10.1103/PhysRevLett.117.013002, which includes Refs. [31–41], for full description of the fit procedure, a further analysis and discussion of the solvent and structural contribution to the difference scattering signal as a function of laser power and an extended description of the dynamics observed in the data, including movies S1 and S2 showing the identified vibrational modes. Details of the IRF-determination and MD simulations are also included.
[32] J. Als-Nielsen and D. McMorrow, *Elements of Modern X-ray Physics* (John Wiley & Sons, New York, 2011), p. 1.
[33] S. Palese, L. Schilling, R. J. D. Miller, P. R. Staver, and W. T. Lotshaw, J. Phys. Chem. **98**, 6308 (1994).
[34] H. W. Horn, W. C. Swope, J. W. Pitera, J. D. Madura, T. J. Dick, G. L. Hura, and T. Head-Gordon, J. Chem. Phys. **120**, 9665 (2004).
[35] W. L. Jorgensen, D. S. Maxwell, and J. Tirado-Rives, J. Am. Chem. Soc. **118**, 11225 (1996).
[36] G. J. Martyna, M. L. Klein, and M. Tuckerman, J. Chem. Phys. **97**, 2635 (1992).
[37] J. Neuefeind, C. J. Benmore, J. K. R. Weber, and D. Paschek, Mol. Phys. **109**, 279 (2011).
[38] F. Neese, Max-Planck-Institut für Chemische Energiekonversion, ORCA version 3.0.3, https://orcaforum.cec.mpg.de/.
[39] F. Neese, WIREs Comput. Mol. Sci. **2**, 73 (2012).
[40] A. D. Becke, Phys. Rev. A **38**, 3098 (1988).
[41] J. P. Perdew, Phys. Rev. B **33**, 8822 (1986).
[42] R. A. Binstead and J. K. Beattie, Inorg. Chem. **25**, 1481 (1986).
[43] A. Dohn, E. Biasin, K. Haldrup, M. M. Nielsen, N. E. Henriksen, and K. B. Møller, J. Phys. B **48**, 244010 (2015).
[44] M. Cammarata, M. Lorenc, T. Kim, J. Lee, Q. Kong, E. Pontecorvo, M. L. Russo, G. Schiro, A. Cupane, M. Wulff *et al.*, J. Chem. Phys. **124**, 124504 (2006).
[45] K. S. Kjaer, T. B. van Driel, J. Kehres, K. Haldrup, D. Khakhulin, K. Bechgaard, M. Cammarata, M. Wulff, T. J. Sørensen, and M. M. Nielsen, Phys. Chem. Chem. Phys. **15**, 15003 (2013).
[46] T. J. Sørensen and K. S. Kjær, https://sites.google.com/site/trwaxs/ (2013).
[47] S. Jun, J. H. Lee, J. Kim, J. Kim, K. H. Kim, Q. Kong, T. K. Kim, M. Lo Russo, M. Wulff, and H. Ihee, Phys. Chem. Chem. Phys. **12**, 11536 (2010).
[48] G. Auböck and M. Chergui, Nat. Chem. **7**, 629 (2015).
[49] C. Consani, M. Prémont-Schwarz, A. ElNahhas, C. Bressler, F. van Mourik, A. Cannizzo, and M. Chergui, Angew. Chem. **121**, 7320 (2009).
[50] G. Vankó *et al.*, J. Phys. Chem. C **119**, 5888 (2015).
[51] X. Zhang, M. L. Lawson Daku, J. Zhang, K. Suarez-Alcantara, G. Jennings, C. A. Kurtz, and S. E. Canton, J. Phys. Chem. C **119**, 3312 (2015).
[52] A. O. Dohn, E. Örn Jónsson, K. S. Kjær, T. B. van Driel, M. M. Nielsen, K. W. Jacobsen, N. E. Henriksen, and K. B. Møller, J. Phys. Chem. Lett. **5**, 2414 (2014).

Supplemental Material for: Femtosecond X-ray scattering study of ultrafast photoinduced structural dynamics in solvated $[Co(terpy)_2]^{2+}$

Elisa Biasin,[1] Tim Brandt van Driel,[1] Kasper S. Kjær,[1,2,3] Asmus O. Dohn,[4] Morten Christensen,[1] Tobias Harlang,[2] Pavel Chabera,[2] Yizhu Liu,[2,5] Jens Uhlig,[2] Mátyás Pápai,[4,6] Zoltán Németh,[6] Robert Hartsock,[3] Winnie Liang,[3] Jianxin Zhang,[7] Roberto Alonso-Mori,[8] Matthieu Chollet,[8] James M. Glownia,[8] Silke Nelson,[8] Dimosthenis Sokaras,[8] Tadesse A. Assefa,[9] Alexander Britz,[9] Andreas Galler,[9] Wojciech Gawelda,[9,10] Christian Bressler,[9] Kelly J. Gaffney,[3] Henrik T. Lemke,[8,11] Klaus B. Møller,[4] Martin M. Nielsen,[1] Villy Sundström,[2] György Vankó,[6] Kenneth Wärnmark,[5] Sophie E. Canton,[12,13] and Kristoffer Haldrup[1]

[1] *Technical University of Denmark, Department of Physics, Fysikvej 307, DK-2800 Kongens Lyngby, Denmark.*

[2] *Department of Chemical Physics, Lund University, Box 118, S-22100 Lund, Sweden.*

[3] *PULSE Institute, SLAC National Accelerator Laboratory, Menlo Park, CA 94025, USA.*

[4] *Technical University of Denmark, Department of Chemistry, Kemitorvet 207, DK-2800 Kongens Lyngby, Denmark.*

[5] *Centre for Analysis and Synthesis, Department of Chemistry, Lund University, Box 124, Lund SE-22100, Sweden.*

[6] *Wigner Research Centre for Physics, Hungarian Academy Sciences, H-1525 Budapest, Hungary.*

[7] *School of Environmental and Chemical Engineering, Tianjin Polytechnic University, Tianjin 300387, China*

[8] *LCLS, SLAC National Accelerator Laboratory, Menlo Park, CA 94025, USA.*

[9] *European XFEL GmbH, Albert-Einstein-Ring 19, D-22761 Hamburg, Germany.*

[10] *Institute of Physics, Jan Kochanowski University, 25-406 Kielce, Poland.*

[11] *SwissFEL, Paul Scherrer Institut, 5232 Villigen PSI, Switzerland.*

[12] *IFG Structural Dynamics of (Bio)chemical Systems, Max Planck Institute for Biophysical Chemistry, Am Fassberg 11, D-37077 Goettingen, Germany*

[13] *FS-SCS, Structural Dynamics with Ultra-short Pulsed X-rays,*
Deutsches Elektronen-Synchrotron (DESY),
Notkestrasse 85, D-22607 Hamburg, Germany

CONTENTS

I. MODEL AND FIT OF THE DATA

As described in the article, the measured difference scattering signal is modelled as

$$\Delta S_{model}(Q,\, t) = \alpha(t)\Delta S_{str.}(Q,\, t) + \Delta S_{solvent}(Q,t) \tag{S1}$$

where $\Delta S_{str.}(Q,\, t) = \Delta S_{solute}(Q,\, t) + \Delta S_{cage}(Q)$, arising from the structural response of the system, and $\Delta S_{solvent}(Q,t) = \Delta T(t)\frac{\partial S(Q)}{\partial T}\Big|_{\rho} + \Delta\rho(t)\frac{\partial S(Q)}{\partial \rho}\Big|_{T}$, describing the changes in X-ray scattering arising from the temperature increase and the density changes of the bulk solvent. In this expression, α represents the excitation fraction and ΔT and $\Delta\rho$ the increase in solvent temperature and density, respectively.

A. Bulk solvent contributions

Fig.S1(a) shows the solvent contributions to the difference scattering signal: $\left.\frac{\partial S(Q)}{\partial T}\right|_{\rho}$ and $\left.\frac{\partial S(Q)}{\partial \rho}\right|_{T}$ from [1, 2]. Fig. S1(b) shows ΔT and $\Delta\rho$ obtained as a function of time when using the expression in Eq. S1 to fit the experimental data presented in the article (Fig.2 (a)). We note that the solvent contribution to the recorded difference scattering signal is completely dominated by the change in scattering arising from the temperature increase, while the contribution from density changes is found to be negligible (less then 0.025 kg·m^{-3}). Therefore, only the former was used in the analysis (Eq.6).

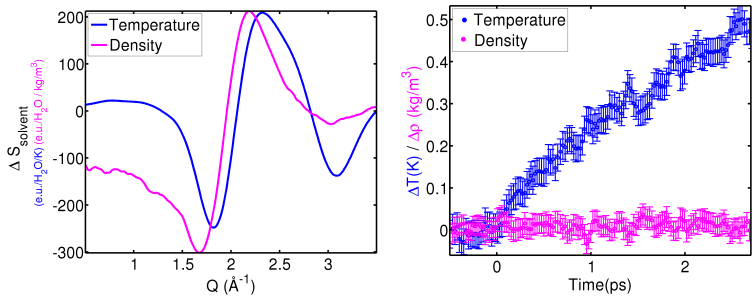

Figure S1. **a:** Measured solvent differentials for water describing the change in difference scattering signal arising from change in temperature (blue) and density (magenta), from [2]. **b:** Fit results for ΔT and $\Delta\rho$ obtained when fitting Eq. S1 to the experimental data in Fig.2(a).

B. Structure and excitation fraction

The scattering signal from the solute molecule (Eq.3) is calculated through the Debye equation:

$$S(Q) = \sum_{i}^{N} |f_i(Q)|^2 + 2\sum_{i<j}^{N} f_i(Q) f_j(Q) \frac{\sin(Q r_{ij})}{Q r_{ij}} \tag{S2}$$

where N is the number of atoms in the molecule, $f_i(Q)$ the atomic form factor for atom i and r_{ij} describe the inter-atomic distances [3].

As discussed in our previous work [4], a strong correlation is often found between the excitation fraction and the magnitude of the structural changes when expressions such as Eq. S1 are used to fit the acquired difference signals. In the present analysis, the simultaneous

determination of both the excitation fraction α and the structural parameter $d_{\text{Co-N}}$ in Eq.6 is significantly improved by assuming the temporal profile of α (Eq.7) and simultaneously optimizing the excited-state molecular structure in a 'global' framework that includes all time delays in the structural analysis [5].

With respect to Eq.7 in the main text, the full expression used to describe the temporal evolution of the the excitation fraction is:

$$\alpha(\mathrm{t}) = \int_{-\infty}^{+\infty} \frac{1}{\sigma_{\text{IRF}}\sqrt{2\pi}} e^{\frac{-(\mathrm{t}-y)^2}{2\sigma_{\text{IRF}}^2}} H(y-\mathrm{t}_0) A e^{-\frac{y-\mathrm{t}_0}{\tau}} dy \tag{S3}$$

where σ_{IRF} is the width of the Gaussian IRF, A and τ are the amplitude and the lifetime of the exponential function, describing respectively the initial amplitude (excitation fraction) and subsequent decay of the bond-elongated excited state, t_0 is the starting point of the exponential decay and y is the integration variable.

Fig.3 of the main article shows the changes in the axial Co-N distance after photoexcitation. The time evolution of this parameter is well described by two oscillations superimposed on an exponential decay, all convoluted with the Gaussian IRF of width σ_{IRF}:

$$\begin{aligned}
\Delta d_{\text{Co-Naxial}}(\mathrm{t}) &= \mathrm{IRF}(\sigma_{\text{IRF}}, \mathrm{t}) \otimes [E e^{-\frac{\mathrm{t}-\mathrm{t}_0}{\tau_R}} + B_1 e^{-\frac{\mathrm{t}-\mathrm{t}_0}{\tau_O}} \cos(\frac{2\pi(\mathrm{t}-\mathrm{t}_0)}{T_1} + f_1) + \\
&\quad + (1 - e^{-\frac{\mathrm{t}-\mathrm{t}_0}{\tau_O}}) B_2 \cos(\frac{2\pi(\mathrm{t}-\mathrm{t}_0)}{T_2} + f_2)] \cdot H(\mathrm{t}-\mathrm{t}_0) \\
&= \int_{\mathrm{t}_0}^{+\infty} \frac{1}{\sigma_{\text{IRF}}\sqrt{2\pi}} e^{-\frac{(\mathrm{t}-y)^2}{2\sigma_{\text{IRF}}^2}} [E e^{-\frac{y-\mathrm{t}_0}{\tau_R}} + B_1 e^{-\frac{y-\mathrm{t}_0}{\tau_O}} \cos(\frac{2\pi(y-\mathrm{t}_0)}{T_1} + f_1) + \\
&\quad + (1 - e^{-\frac{y-\mathrm{t}_0}{\tau_O}}) B_2 \cos(\frac{2\pi(y-\mathrm{t}_0)}{T_2} + f_2)] dy
\end{aligned} \tag{S4}$$

where E and τ_R are the amplitude and the lifetime of the exponential decay, B_1, T_1 and f_1 are, respectively, the amplitude, the period and the phase of the first oscillation, and B_2, T_2 and f_2 are, respectively, the amplitude, the period and the phase of the second oscillation. τ_O is the dampening time of the first oscillation as well as the grow-in time of the second one, and y is the integration variable. The best-fit parameters obtained by fitting this expression to $\Delta d_{\text{Co-Naxial}}$ are reported in Table S1. The (adjusted) R^2 is found 0.88. We note that E describes the difference between $d_{\text{Co-Naxial}}$ of the bond-elongated excited state at time zero and the average value of the same quantity after 2 ps. This latter value for $d_{\text{Co-Naxial}}$ is interpreted as the axial Co-N bond length of the HS structure and used in the fit of the long time range dataset (Section V).

σ_{IRF} (ps)	0.05 (fixed)
t_0 (ps)	-0.01 (fixed)
E (Å)	0.014 ± 0.002
τ_R (ps)	0.7 ± 0.1
B (Å)	0.03 ± 0.01
τ_O (ps)	0.4 ± 0.1
T (ps)	0.33 ± 0.03
f (a.u)	- 4.4 ± 0.4
B_2 (Å)	0.002 ± 0.003
T_2 (ps)	0.23 ± 0.01
f_2 (a.u)	0.7 ± 0.7

Table S1. Fit results (95 % confidence bounds) after fitting the expression in Eq. S4 to $\Delta \mathrm{d}_{\text{Co-Naxial}}(\mathrm{t})$ (Fig.3).

C. Bulk solvent kinetics

Fig. S2 shows the temporal evolution of $\Delta\mathrm{T}(\mathrm{t})$ (black points). The data are described through the expression:

$$\Delta \mathrm{T}(\mathrm{t}) = \mathrm{IRF}(\sigma_{\mathrm{IRF}}, \mathrm{t}) \otimes H(\mathrm{t}-\mathrm{t}_0) \sum_{j=1}^{N} \gamma_j (1 - e^{-\frac{\mathrm{t}-\mathrm{t}_0}{\tau_j}}) \tag{S5}$$

$$= \int_{\mathrm{t}_0}^{+\infty} \frac{1}{\sigma_{\mathrm{IRF}}\sqrt{2\pi}} e^{-\frac{(\mathrm{t}-y)^2}{2\sigma_{\mathrm{IRF}}^2}} \sum_{j=1}^{N} \gamma_j (1 - e^{-\frac{y-\mathrm{t}_0}{\tau_j}}) dy$$

where σ_{IRF} is the width of the Gaussian IRF, γ and τ are the amplitude and the lifetime of the N exponential functions and H is the Heaviside step function centered at t_0. Fig. S2 shows a comparison between using a single (N=1) or a double (N=2) exponential function to describe the short time range dataset and we find that the latter better describes the time evolution of ΔT in the first hundreds of femtoseconds. A single exponential grow-in is used to fit the long time range measurements (see Fig. S8). The parameters obtained for both datasets are reported in Tab. S2.

	short time range	long time range
σ_{IRF} (ps)	0.05 (fixed)	0.05 (fixed)
t_0 (ps)	-0.01 (fixed)	-0.01 (fixed)
γ_1 (K)	0.05 $\pm$ 0.2	/
τ_1 (ps)	0.01 $\pm$ 0.9	/
γ_2 (K)	0.8 $\pm$ 0.3	0.84 $\pm$ 0.02
τ_2 (ps)	3.5 $\pm$ 0.8	4.0 $\pm$ 0.6

Table S2. Fit results (95 % confidence bounds) after fitting the expression in Eq. S5 to ΔT(t) both in the short (Fig.S2) and the long (Fig. S8(b)) time range.

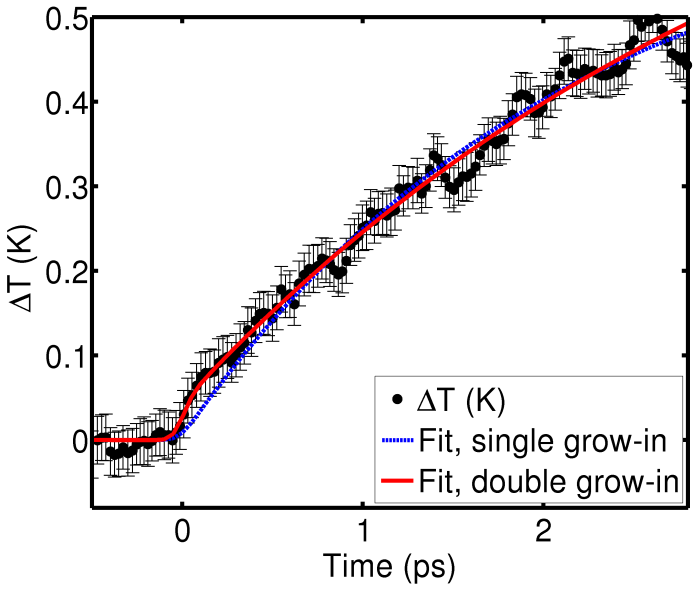

Figure S2. Time evolution of the temperature increase ΔT of the bulk-solvent modelled as a single (dashed blue) or a double (red) exponential grow-in (Eq. S5).

D. Error estimates

As utilized in our previous analysis of XDS data and described in detail in [4], the difference signal ΔS is known to be varying only slowly as a function of Q. We estimate the noise for each ΔS(Q,t) point from the high frequency fluctuations present in an interval around that point. Specifically, for every data point Q_p in the Q-range (with a total number

of $N = 500$ points), we fit a third-order polynomial to ΔS in a 50-point Q-interval around Q_p and estimate the noise σ at Q_p as the standard deviation of the residuals between data and polynomial fit in this interval.

The 'global' fitting procedure was implemented in Matlab®, utilizing constrained minimization of the standard χ^2 estimator:

$$\chi^2(\alpha, d_{\text{Co-Naxial}}, \Delta T) = \Big(\sum_{p=1}^{N} \frac{(\Delta S(Q_p)_{\text{model}} - \Delta S(Q_p)_{\text{meas.}})^2}{\sigma(Q_p)^2}\Big) \cdot \frac{1}{N - P - 1}. \qquad \text{(S6)}$$

where P is the number of free parameters.

The uncertainty estimates for $d_{\text{Co-Naxial}}$ and ΔT for each time point were calculated from the Hessian matrix returned by Matlab®. In the representation shown in Fig. 3 of the main article, $d_{\text{Co-Naxial}}$ was smoothed by a 4-point nearest neighbour filter (∼100 fs), reducing the estimated uncertainty on each point by a factor of two. The uncertainty on the initial excitation fraction A in Eq.7 was estimated as follows. A was allowed to range freely with the remaining fit parameters locked to their best-fit value, thus producing a 2D $\Delta S_{\text{model}}(Q,t)$ matrix for each value of the free parameter from which an average χ^2 could be computed by direct comparison with the measured data set through Eq. S6. These $\chi^2(A)$ curves were converted to a (relative) likelihood distribution $L(A)$ through $L = exp(-\chi^2/2)$ [5]. $L(A)$ was subsequently fitted with a Gaussian, and the error estimated as the σ of this Gaussian function [4].

II. ANISOTROPIC SIGNAL $\Delta S_{\text{ani.}}(Q,T)$ AND ESTIMATE OF σ_{IRF}

Fig. S3(a) shows the anisotropic contribution ($\Delta S_{\text{ani.}}$) to the total difference scattering signal, with the isotropic part (ΔS) shown in Fig. 2 and analysed in the main text. The two contributions were extracted from the 2D difference scattering patterns as detailed in [6]. As the excitation of the solute molecules have very little or no polarization dependence, the anisotropic component of the difference scattering signal arises from the almost instantaneous transient response of the water molecules to the electric field of the laser pulse (Kerr effect). The very fast nature of this response [7] allows us to use it to estimate the time resolution of the experiment. The response is found to be well described by the convolution of an exponential decay with a Gaussian IRF, and by fitting this model to the data we find σ_{IRF} = 0.05 ± 0.03 ps and t_0 = -0.01 ± 0.03 ps (see Fig. S3(b)). These values are assumed to

describe the IRF for the experiments presented in this work, and were kept fixed throughout the analysis described in the main text.

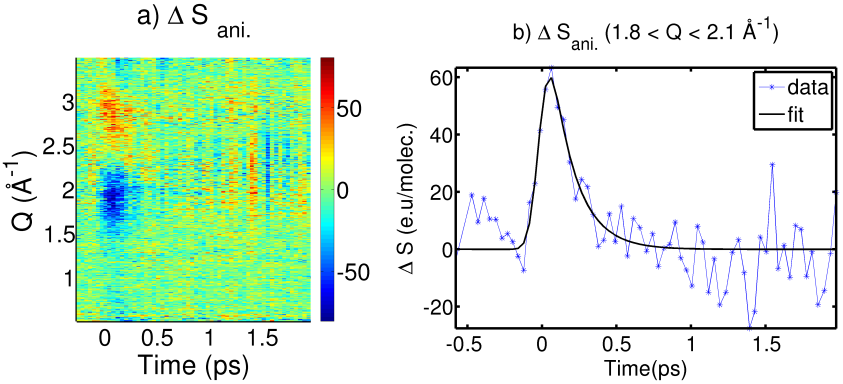

Figure S3. **a:** Anisotropic difference scattering signal $\Delta S_{ani.}(Q,t)$. **b:** Averaged value of $\Delta S_{ani.}$ in the interval 1.8 Å $< Q <$ 2.1 Å, where the scattering signature of the transient alignment of water molecules with the polarized laser pulse appears is most dominant. The expression in Eq. S3 is used for the fit.

III. SVD ANALYSIS

Fig. S4(a) shows the difference scattering signal $\Delta S_{Solv\text{-}subtr.}$ obtained after subtracting the (fitted, see above and main text for details) solvent contribution from ΔS (Q,t) (Fig.2). It is dominated by the negative feature at low-Q, signature of the expansion of the Co-N bonds. Fig. S4(b, c and d) show the main results of a Singular Value Decomposition (SVD) of this signal. As indicated by the relative magnitude of the singular values shown in Fig. S4(b), a single component dominates the signal. This component and its amplitude as a function of time are shown in Fig. S4(c) and Fig. S4(d), respectively.

With respect to the latter, the time evolution arises from both the structural dynamics and the kinetics of the bond-elongated state. Fig.S5 shows that, up to 0.5 ps, this time evolution is well-described by a grow-in exponential function followed by an oscillation, all broadened by the IRF:

$$V_1^{model}(t) = IRF(\sigma_{IRF}, t) \otimes [R(1 - e^{-\frac{t-t_0}{\tau_G}}) + O\cos(\frac{2\pi(t-t_0)}{T} + f)] \cdot H(t-t_0) \qquad (S7)$$

$$= \int_{t_0}^{+\infty} \frac{1}{\sigma_{IRF}\sqrt{2\pi}} e^{-\frac{(t-y)^2}{2\sigma_{IRF}^2}} [R(1 - e^{-\frac{y-t_0}{\tau_G}}) + O\cos(\frac{2\pi(y-t_0)}{T} + f)]dy$$

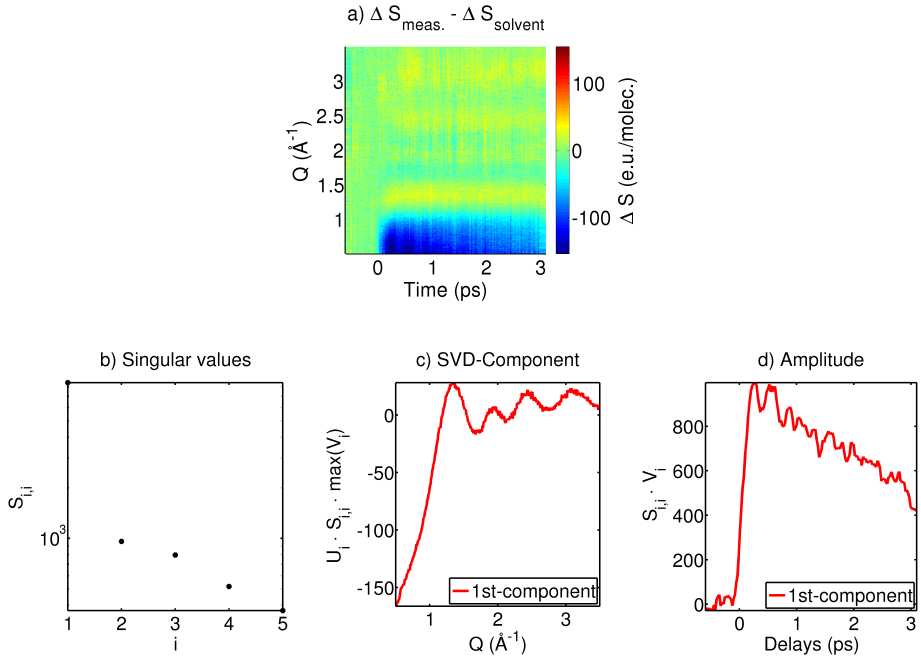

Figure S4. **a:** $\Delta S_{\text{Solv-subtr.}}$: difference scattering signal obtained by subtracting $\Delta S_{\text{solvent}}$ from the experimental data. **b-d:** Results of a SVD analysis of the data in **a**. $\Delta S_{\text{Solv-subtr.}} = U \cdot S \cdot V^{T}$. **b:** The singular values of the diagonal $S_{i,i}$. **c:** Q-profile of the first component ($U_1 \cdot S_{1,1} \cdot max(V_1)$). **d:** Temporal evolution of the first component ($S_{1,1} \cdot V_1$), smoothed by a 3-point nearest neighbour filter (∼75 fs).

where R and τ_G are the amplitude and the lifetime of the exponential, and O, T and f the amplitude, the period and the phase of the oscillation, respectively, and y is the integration variable. The values of both the fixed variables and the obtained parameters are reported in Tab. S3. The rise time of the structural signal is found to be 0.06 ps ± 0.01 ps and the phase shift of the oscillation, which has a period of ∼0.33 ps, is found to be 0.08 ps ± 0.02 ps. This is interpreted as an indication of the presence of one (or more) intermediate state(s) before the (electronic) population of the bond-elongated state, as further discussed in the main text.

σ_{IRF} (ps)	0.05 (fixed)
t_0 (ps)	-0.01 (fixed)
R (a.u.)	0.91 ± 0.03
τ_G (ps)	0.06 ± 0.01
O (a.u.)	0.09 ± 0.06
T (ps)	0.33 (fixed)
f (a.u.)	1.5 ± 0.4

Table S3. Fit results (95 % confidence bounds) after fitting the expression in Eq. S7 to the (normalized) amplitude of the first component after a SVD of $\Delta S_{\text{Solv-subtr.}}$ (Fig. S5).

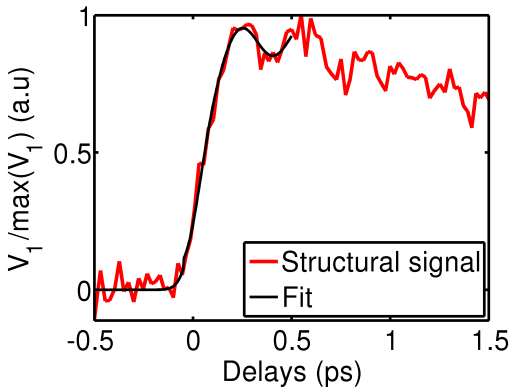

Figure S5. Temporal evolution of the (normalized) amplitude of the first component obtained from a SVD analysis of $\Delta S_{\text{Solv-subtr.}}$ (Fig. S4). We interpret this as the signal arising from primarily the change in the structure of the solute. The black line represents a fit to the data, utilizing a IRF-broadened exponential grow-in function with lifetime of 0.06 ps ± 0.01 ps followed by an oscillation of 0.33 ps period and with a 0.08 ps ± 0.02 ps phase shift.

IV. FOURIER TRANSFORM OF THE OSCILLATORY STRUCTURAL SIGNAL

Fig.S6(a) shows the temporal evolution of the structural contribution (red line) to the measured ΔS (see Fig. S4). This temporal evolution is described by a broadened exponential decay (black line). The residuals (blue line) between the data and the fit are here referred to as the oscillatory structural signal (OSS). Fig.S6(b) shows the Fourier Transform of the OSS for t > 0.3 ps: two main peaks are found at ∼0.23 ps and ∼0.34 ps. The inset of Fig.3

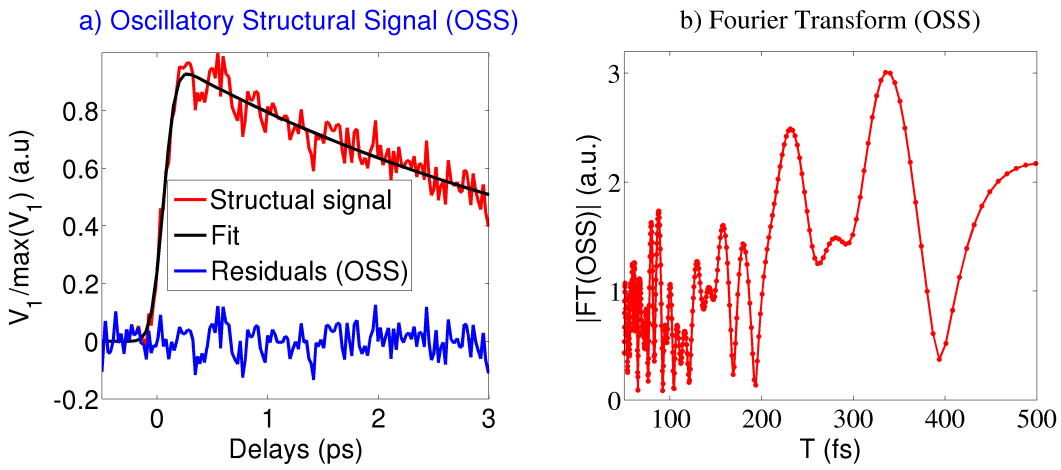

Figure S6. **a:** Amplitude of the first SVD component of $\Delta S_{Solv-subtr}$ (see Fig. S4) as a function of time (red). This represents the time evolution of the structural signal. An exponential decay broadened by a Gaussian function (black) is fitted to the data. Difference (blue) between the structural signal and the exponential fit. We refer to this as the oscillatory structural signal (OSS). **b:** Fourier Transform (FT) of the OSS for t > 0.3 ps, with the two main peaks at 220 fs and 340 fs.

in the main article shows the time dependent FT of the OSS obtained by sliding a 2 ps Hann window starting from a central value of 0.6 ps up to a central value of 2 ps.

V. LONG TIME RANGE MEASUREMENTS

Fig. S7(a) shows the isotropic difference scattering signals $\Delta S(Q, t)$ measured for time delays up to 20 ps. This dataset was binned in ∼300 fs bins, with 400 images in each bin. The following model was used to fit the data at each time delay:

$$\Delta S_{\text{model}}(Q, t) = \alpha(t)\Delta S_{\text{str.}}(Q) + \Delta T(t)\frac{\partial S(Q)}{\partial T}\bigg|_{\rho} \tag{S8}$$

with α and ΔT as free parameters and $\Delta S_{\text{struc.}}$ calculated from the structure of $[Co(terpy)_2]^{2+}$ 2 ps after the photoexcitation (as obtained from the analysis of the short time range dataset). This model can describe the data at all time delays, as indicated by the low residuals in Fig. S7(b). The time evolution of the kinetic parameters, α and ΔT are reported in Fig. S8. A single exponential decay is used to fit the excitation fraction α after 2 ps (i.e. after the excited-state structure has relaxed), and a lifetime of 6.8 ps ± 0.8 ps is found. The

temporal evolution of the temperature increase is well-described by a single exponential grow-in function (Eq. S5) and the obtained parameters are reported in Tab. S2.

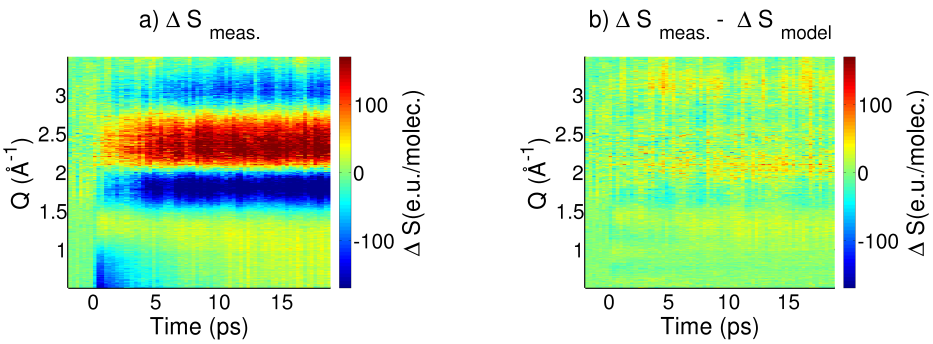

Figure S7. **a:** Measured difference scattering signal ($\Delta S_{meas.}(Q, t)$) of photoexcited $[Co(terpy)_2]^{2+}$ in aqueous solution (long time range dataset). **b:** Residuals obtained by subtracting the model (Eq. S8) from the experimental data.

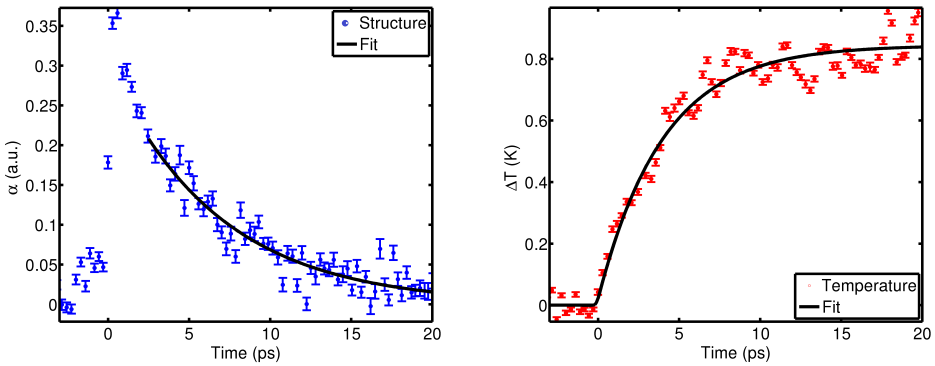

Figure S8. Kinetics obtained from the fit of the long time range dataset. **a:** Evolution of α, the magnitude of the structural component observed in the difference scattering signal (blue points). After 2 ps, it is well-described by an exponential decay with lifetime of 6.8 ps ± 0.8 ps (black line), interpreted as the lifetime of the bond-elongated HS excited state. **b:** Time evolution of the temperature increase ΔT of the solvent (red points). The temperature increase is well described by an exponential grow-in with a time constant of 4.0 ps ± 0.6 ps (Eq. S5).

VI. MD SIMULATIONS AND RDF ANALYSIS

The LS and HS structures of $[Co(terpy)_2]^{2+}$ were solvated in a cubic box (50 Å size) of water molecules using the TIP4P-Ew potential [8]. The bond lengths of the solute molecule were constrained and MD trajectories were calculated with OPLS2005 force field parameters [9] and a Nose-Hoover thermostat at 300 K [10]. The Radial Distribution Functions (RDFs) of the solute-solvent atom pairs were sampled in 0.1 Å radial bins and over 2000 individual simulation time steps over a total time interval of 2 ns. Fig. S9 shows the radial distribution functions (RDFs) g(r) of the oxygen (O) and hydrogen (H) atoms with respect to the Co atom, r being the distance from the Co, and the coordination number cn(r), the number of oxygens/hydrogens contained in a sphere of radius r, for both the LS and HS states of solvated $[Co(terpy)_2]^{2+}$. The first peak in the RDFs represents the first solvation shell. By inspection of $g_{CoO}(r)$ in Fig. S9(a), we note that the first peak slightly shifts (∼0.1 Å) towards smaller r values, decreases in amplitude and broadens upon the LS → HS spin transition on the Co centre. Considering the first minimum in the RDFs to be the limit of the first solvation shell, in the LS state it is found at 5.9 Å and, at this value, cn(r) is found to be ∼12 for both spin states. Similar considerations for $g_{CoH}(r)$ are shown in Fig. S9(b). This observation indicates that, upon the expansion of the Co-N bonds, the water molecules on average come closer (∼ 0.1 Å) to the Co-center but their total number in the first solvation shell remains constant. Finally, Fig. S9(c) shows that, relative to the H, the O come slightly closer to the positive Co centre in the HS spin with respect to the LS spin, representing a general rotation of the water molecules upon the spin transition.

VII. ENERGETICS

The laser pump energy absorbed by the solute molecules and the subsequent temperature increase of the solvent due to non-radiative relaxation of the solute can be estimated from experimental parameters, as detailed in [1]. Given a square X-ray spot size of $d_{X\text{-ray}} = 50$ μm, a path length (through the 45 ° tilted liquid sheet) of $l = 140$ μm and a sample concentration of $c = 20$mM, the number of molecules N_V in the probed volume can be calculated as:

$$N_V = c \cdot N_A \cdot d_{X\text{-ray}}^2 \cdot l = 4.2 \cdot 10^{12}$$

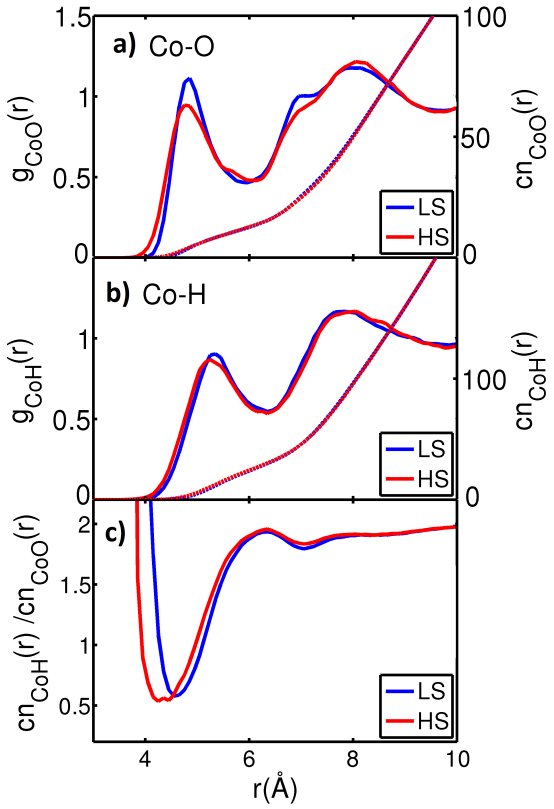

Figure S9. **a-b:** LS and HS RDFs g(r) of the water oxygen (**a**) and hydrogen (**b**) atoms with respect to the Co atom (solid line, left y-axis) and coordination number cn(r) (dashed lines, right y-axis) **c:** ratio of the Co-H to the Co-O coordination number in the LS and HS state, describing the orientation of the water molecules with respect to the Co center.

where N_A is Avogadro's number. Given an excitation fraction of 34 %, as found in our analysis, the number of excited molecule is then:

$$N_{\text{exc.}} = 0.34 \cdot N_V = 1.4 \cdot 10^{12}.$$

By assuming a linear regime such that each of these molecules absorbed one 530 nm photon (2.3 eV per photon), the energy per unit volume released to the solvent after non-radiative decay of the solute species would be:

$$E_{\text{dep.}} = \frac{N_{\text{exc.}} \cdot 2.3 \text{ eV}}{(50 \text{ cm})^2 \cdot l} = 1.5 \text{ J/cm}^3.$$

The specific heat capacity of water is $C_p = 4.18$ J$\cdot$ cm^{-3} $\cdot$ K^{-1} and the average temperature change in the volume probed by the X-ray would then be expected to be:

$$\Delta T = \frac{E_{\text{dep.}}}{C_p} = 0.38 \text{ K}$$

which is lower than the 0.84 K found from the analysis of the experimental dataset (Tab. S2). This we interpret as an indication that multi-photon excitation of the sample (solute and solvent) may be present and should be taken into account in the analysis. That such higher-order processes appear to be active is not surprising, as the excitation laser intensity is quite high. Given a laser pulse length of 70 fs and a laser pulse energy of 70 μJ focused on a spot of diameter of $d = 150$ μm (FHWM), the peak irradiance will be 3.5 TW/cm^2.

In order to further investigate the robustness of the results presented in the main article in the presence of multi-photon absorbtion, a second dataset with significantly lower laser power, 20 μJ (i.e. at a peak irradiance of 1 TW/cm^2), was subjected to the same analysis as that presented in the main text (Eq.5). For this dataset, we find an excitation fraction of 19 % and a 0.2 K temperature increase, as shown in Fig.S10(a). From the same energetics calculations as above, a temperature increase of 0.2 degrees indicates that the 20 μJ data set represents the response in the linear, one-photon excitation regime. Fig.S10(b) shows that the Co-N bond length dynamics results obtained from the analysis of the 20μJ dataset are essentially the same, but with more noise, than those obtained from the 70μJ dataset and presented in the main article.

As discussed in detail in our previously published LCLS studies, the presence of multi-photon excitation can result in very significant local heating of the solvent [11]. This may in turn lead to a breakdown in the assumption that the changes in scattering due to the temperature response of the aqueous solvent can be well described by a single, linearly scaled solvent differential. However, as also described in our recent work [11], the model describing the changes in solvent scattering can be readily extended to include a second-order term $\left.\frac{\partial^2 S(Q)}{\partial T^2}\right|_\rho$ which can be obtained from either MD modelling or from experiments [12]. Including this contribution in the full model, we found that it contributed at most 5 % of the measured difference signal and it was found to have no discernible impact on any of the results presented in this work. Including the second order solvent differential in the analysis of the 20 μJ indicated no contribution.

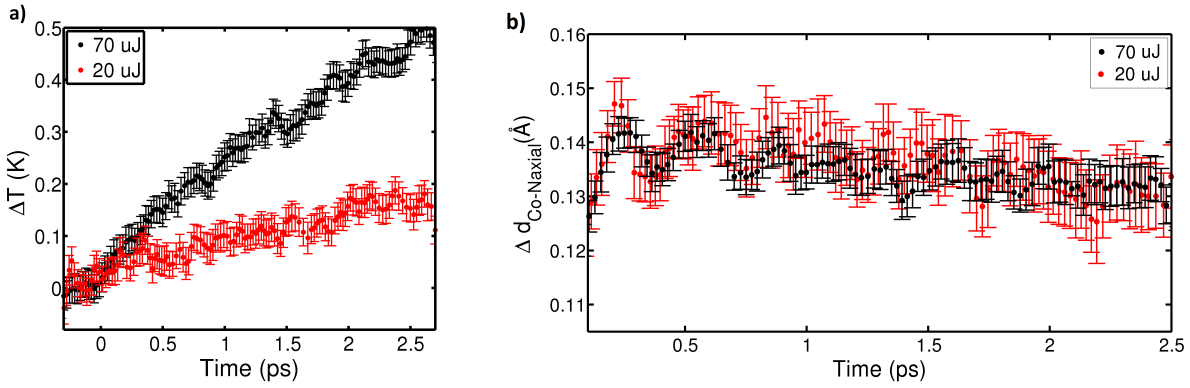

Figure S10. **a:** Time evolution of the temperature increase of the bulk-solvent after photoexcitation of the sample with a 20 μJ (red) or a 70 μJ (black) laser pulse. **b:** Time evolution of the changes in the Co-N bond length distance from the ground to the excited state after after photoexcitation with a 20 μJ (red) or a 70 μJ (black) laser pulse.

VIII. DFT CALCULATIONS

The DFT calculations were carried out with the ORCA program package [13, 14], utilizing the gradient-corrected BP86 exchange correlation functional [15, 16] in combination with the TZVP basis set. Solvent effects were approximated by the application of the conductor-like screening model (COSMO) using the relative permittivity of water ($\varepsilon = 80.4$). Vibrational frequencies were calculated as second derivatives of the electronic energy, and were all found to be positive, confirming that the optimized geometries at the BP86/TZVP level correspond to true minima of the corresponding potential energy surfaces (PES). Movie S1 shows the breathing mode of the HS state of $[Co(terpy)_2]^{2+}$, using the vectors and the frequency (92 cm^{-1}) obtained from DFT calculation. From the same calculation, Movie S2 shows the 'pincer-like' mode found at 146 cm^{-1}.

IX. EXPERIMENTAL SETUP AND DATA REDUCTION

The 20 mM aqueous solution of $Co(terpy)_2Cl_2$ was prepared according to the procedure given in [17]. Fig.S11 shows the absorption spectrum of $[Co(terpy)_2]^{2+}Cl_2$ in water. For the experiment, the solution was pumped through a sapphire nozzle producing a 100 µm flat liquid sheet flowing in the vertical direction and inclined at 45° to the (nearly) collinear

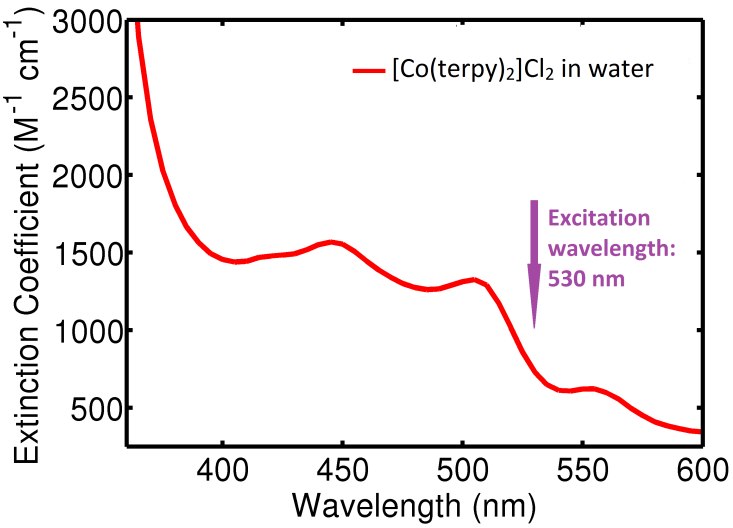

Figure S11. UV-Vis absorption spectrum of $[Co(terpy)_2]^{2+}$ in water.

co-propagating laser and X-ray beams. The flow rate (ca. 1 mm/ms) was sufficient to fully replace the sample between successive X-ray pulses at the 120 Hz repetition rate of the LCLS facility. The laser system produced 70 μJ pulses at 530 nm with 70 fs pulse width (FWHM) and 7.5 nm bandwidth (FWHM). It was focused onto a 150 μm diameter spot (via a CaF_2 lens with 750 mm focal length). The 8.3 keV X-ray probe pulses (with $\sim 10^{12}$ photons/pulse on average) were focused to a (50 μm)^2-size square spot and overlapped with the pump laser at the sample position. The laser excited the sample synchronously for every probing X-ray pulse, except for every 5th pulse, where the laser beam was dropped before the sample position, so that the static structure of the sample with only ground state species present could be repeatedly measured during the sequence of pump-probe XDS measurements. The acquired 2D scattering patterns were corrected for artefacts due to X-ray pulse energy and intensity shot-to-shot jitter following the procedure described by van Driel et al. [18]. The patterns were then corrected for X-ray polarization, solid-angle and absorption through the liquid sheet. The radially integrated scattering signal from each pattern was scaled to the total 1D scattering signal calculated in electron units for a liquid unit cell, which, in the present experiment, consists of one solute molecule, 2777 water molecules and two Cl atoms. The full Q range [0.5 - 3.5] $Å^{-1}$ was used as scaling interval and the so-obtained scaling factor was then used to scale each 2D pattern. Individual 2D difference scattering images were obtained by subtracting the laser-off from the laser-on scattering patterns. In

order to extract the temporal behaviour during a time-delay scan between laser and X-ray pulses, the time-corrected images (using the XPP timing tool [19]) were sorted into ∼23 fs wide bins with 600 difference scattering patterns being averaged in each. 1D isotropic and anisotropic difference scattering signals were extracted from each of these averaged 2D difference patterns. For the set of measurements described here, the relative intensity of the difference signal was on the order of 0.1 % of the total scattering signal.

[1] K. S. Kjaer, T. B. van Driel, J. Kehres, K. Haldrup, D. Khakhulin, K. Bechgaard, M. Cammarata, M. Wulff, T. J. Sørensen, and M. M. Nielsen, Physical Chemistry Chemical Physics **15**, 15003 (2013).

[2] T. J. Sørensen and K. S. Kjær, (2013), https://sites.google.com/site/trwaxs/.

[3] J. Als-Nielsen and D. McMorrow, "X-rays and their interaction with matter," in *Elements of Modern X-ray Physics* (John Wiley and Sons, Inc., 2011) pp. 1–28.

[4] K. Haldrup, M. Christensen, and M. Meedom Nielsen, Acta Crystallographica Section A **66**, 261 (2010).

[5] S. Jun, J. H. Lee, J. Kim, J. Kim, K. H. Kim, Q. Kong, T. K. Kim, M. Lo Russo, M. Wulff, and H. Ihee, Physical Chemistry Chemical Physics **12**, 11536 (2010).

[6] U. Lorenz, K. B. Møller, and N. E. Henriksen, New Journal of Physics **12**, 113022 (2010).

[7] S. Palese, L. Schilling, R. J. D. Miller, P. R. Staver, and W. T. Lotshaw, The Journal of Physical Chemistry **98**, 6308 (1994).

[8] H. W. Horn, W. C. Swope, J. W. Pitera, J. D. Madura, T. J. Dick, G. L. Hura, and T. Head-Gordon, The Journal of Chemical Physics **120**, 9665 (2004).

[9] W. L. Jorgensen et al., Journal of the American Chemical Society **118**, 11225–11236 (1996).

[10] G. J. Martyna, M. L. Klein, and M. Tuckerman, The Journal of Chemical Physics **97**, 2635 (1992).

[11] K. Haldrup, W. Gawelda, R. Abela, R. Alonso-Mori, U. Bergmann, A. Bordage, M. Cammarata, S. Canton, A. Dohn, T. van Driel, D. Fritz, A. Galler, P. Glatzel, T. Harlang, K. Kjær, H. Lemke, K. Moller, Z. Németh, M. Pápai, N. Sas, J. Uhlig, D. Zhu, G. Vankó, V. Sundstrom, M. Nielsen, and C. Bressler, The Journal of Physical Chemistry B **120**, 1158 (2016).

[12] J. Neuefeind, C. J. Benmore, J. K. R. Weber, and D. Paschek, Molecular Physics **109**, 279 (2011).

[13] ORCA version 3.0.3, F. Neese, Max-Planck-Institut für Chemische Energiekonversion, https://orcaforum.cec.mpg.de/.

[14] F. Neese, WIREs Computational Molecular Science **2**, 73 (2012).

[15] A. D. Becke, Physical Review A **38**, 3098 (1988).

[16] J. P. Perdew, Physical Review B **33**, 8822 (1986).

[17] R. A. Binstead and J. K. Beattie, Inorganic Chemistry **25**, 1481 (1986).

[18] T. B. van Driel, K. S. Kjaer, E. Biasin, K. Haldrup, H. T. Lemke, and M. M. Nielsen, Faraday Discussions **177**, 443 (2015).

[19] M. P. Minitti, J. S. Robinson, R. N. Coffee, S. Edstrom, S. Gilevich, J. M. Glownia, E. Granados, P. Hering, M. C. Hoffmann, A. Miahnahri, and et al., Journal of Synchrotron Radiation **22**, 526 (2015).